

Global energy spectrum of the general oceanic circulation

Received: 12 April 2022

Accepted: 26 August 2022

Published online: 09 September 2022

 Check for updates

Benjamin A. Storer¹, Michele Buzzicotti², Hemant Khatri³, Stephen M. Griffies⁴ & Hussein Aluie¹ ✉

Advent of satellite altimetry brought into focus the pervasiveness of mesoscale eddies $\mathcal{O}(100)$ km in size, which are the ocean's analogue of weather systems and are often regarded as the spectral peak of kinetic energy (KE). Yet, understanding of the ocean's spatial scales has been derived mostly from Fourier analysis in small "representative" regions that cannot capture the vast dynamic range at planetary scales. Here, we use a coarse-graining method to analyze scales much larger than what had been possible before. Spectra spanning over three decades of length-scales reveal the Antarctic Circumpolar Current as the spectral peak of the global extra-tropical circulation, at $\approx 10^4$ km, and a previously unobserved power-law scaling over scales larger than 10^3 km. A smaller spectral peak exists at ≈ 300 km associated with mesoscales, which, due to their wider spread in wavenumber space, account for more than 50% of resolved surface KE globally. Seasonal cycles of length-scales exhibit a characteristic lag-time of ≈ 40 days per octave of length-scales such that in both hemispheres, KE at 10^2 km peaks in spring while KE at 10^3 km peaks in late summer. These results provide a new window for understanding the multiscale oceanic circulation within Earth's climate system, including the largest planetary scales.

The oceanic circulation is a key component in Earth's climate system. It is both the manifestation and cause of a suite of linear and nonlinear dynamical processes acting over a broad range of spatio-temporal scales¹. The wavenumber spectrum of the oceanic circulation allows us to understand the energy distribution across spatial scales throughout the globe, reveals key bands of scales within the circulation system at which energy is concentrated, and unravels power-law scalings that can be compared to theoretical predictions². The spectrum is an important guide to probing (i) energy sources and sinks maintaining the oceanic circulation at various scales, (ii) how energy is ultimately dissipated, and (iii) how the ocean at a global climate scale is coupled to motions several orders of magnitude smaller.

Thanks to satellite observations^{3,4} and high-resolution models and analysis^{5,6}, it is now well-appreciated that the mesoscales, traditionally thought of as transient eddies of $\mathcal{O}(10^2)$ km in size, form a key band of

spatial scales that pervade the entire ocean and have a leading order effect on the transport of heat, salt, and nutrients, as well as coupling to the global meridional overturning circulation⁷. The mesoscales are generally viewed as forming the peak of the KE spectrum of the oceanic circulation^{1,4,8,9} (e.g., Fig. 5 of ref. 8 or Fig. 5 of ref. 9). However, the existence of the mesoscale spectral peak and the length-scale at which it occurs is not known with certainty¹. Evidence is often derived from performing Fourier analysis on the ocean surface velocity⁶ or sea-surface height¹⁰ within regions that are typically 5° to 10° in extent (nominally 500 to 10^3 km)^{11,12}. The peak appears in only a fraction of the chosen regions, and spectral energy tends to be largest at the largest length-scales (smallest wavenumbers), which are most susceptible to artifacts from the finite size of the chosen regions and the windowing required for Fourier analysis¹. To date, there has been no determination of the oceanic energy wavenumber spectrum at planetary scales.

¹Department of Mechanical Engineering and Laboratory for Laser Energetics, University of Rochester, Rochester, NY, USA. ²Department of Physics, University of Rome Tor Vergata and INFN, Rome, Italy. ³Department of Earth, Ocean and Ecological Sciences, University of Liverpool, Liverpool, UK. ⁴NOAA Geophysical Fluid Dynamics Laboratory and Princeton University Atmospheric and Oceanic Sciences Program, Princeton, NJ, USA. ✉e-mail: hussein@rochester.edu

Do the mesoscales of $\mathcal{O}(10^2)$ km actually form the peak of the ocean's KE spectrum? What is the KE content of scales larger than $\mathcal{O}(10^3)$ km which constitute the ocean's large-scale general circulation (e.g., gyres, western boundary currents, Antarctic Circumpolar Current (ACC)), and are directly coupled to the climate system?

Below, we present the first KE spectrum over the entire range of scales resolved in data from satellites and $1/12^\circ$ -resolution models at the ocean's surface, including the spectrum at planetary scales. We find that the spectral peak of the global extratropical ocean is at $\approx 10 \times 10^3$ km and is due to the ACC. We see vestiges of a similar peak in the northern hemisphere, which is arrested at a smaller amplitude and at smaller scales ($\approx 4 \times 10^3$ km) due to continental boundaries. Another prominent spectral peak is at $\approx 3 \times 10^2$ km, and with an amplitude less than half that of the ACC. Yet, the cumulative energy in the mesoscales between 10^2 km and 5×10^2 km is very large (>50% of total resolved energy). We also report the first observation of a roughly k^{-1} power-law scaling over scales larger than 10^3 km in both hemispheres, consistent with a theoretical prediction from a quasi-geostrophic model forced by wind^{13,14}, with the power-law scaling extending up to the ACC peak in the southern hemisphere.

Our results here open exciting avenues of inquiry into oceanic and climate dynamics, allowing us to seamlessly probe interactions between motions at scales $\mathcal{O}(10^2)$ km and smaller with planetary scales larger than $\mathcal{O}(10^3)$ km. We are able to do so using a coarse-graining approach developed recently to probe multi-scale dynamics on the sphere^{15–17}.

Our methodology, described in the “Methods” section and in refs. 15,16, allows us to coarse-grain the ocean flow at any length-scale of choice and calculate the KE of the resulting coarse flow. By performing a ‘scan’ over an entire range of length-scales, we extract the so-called ‘filtering spectrum’ without needing to perform Fourier transforms¹⁸. The filtering spectrum and the traditional Fourier spectrum agree when the latter is possible to calculate, as demonstrated in ref. 18 and in the Methods section. Unlike traditional Fourier analysis within a box/subdomain, coarse-graining can be meaningfully applied on the entire spherical planet, including land/sea boundaries, and so allows us

to probe everything from the smallest resolved scales up to planetary scales.

Given a velocity field \mathbf{u} and a filter scale ℓ , coarse-graining produces a filtered velocity $\bar{\mathbf{u}}_\ell$ that only contains spatial scales larger than ℓ , having had smaller scales removed (see Fig. 1 and the “Methods” section). Unlike standard approaches to low-pass filtering geophysical flows, such as by averaging adjacent grid-cells or block-averaging in latitude-longitude, the coarse-graining of ref. 16 used here relies on a generalized convolution operation that respects the underlying spherical topology of the planet, thus preserving the fundamental physical properties of the flow, such as its incompressibility, its geostrophic character, and the vorticity present at various scales. The KE (per unit mass, in m^2/s^2) contained in scales larger than ℓ is

$$\mathcal{E}_\ell = \frac{1}{2} |\bar{\mathbf{u}}_\ell(\mathbf{x}, t)|^2 \quad (\text{coarse KE}). \quad (1)$$

While \mathcal{E}_ℓ quantifies the cumulative energy at all scales larger than ℓ , the wavenumber spectrum quantifies the spectral energy density at a specific scale, similar to the common Fourier spectrum. Following¹⁸, we extract the KE content at different length-scales by differentiating the coarse KE with respect to length-scale,

$$\bar{E}(k_\ell, t) = \frac{d}{dk_\ell} \{\mathcal{E}_\ell\} = -\ell^2 \frac{d}{d\ell} \{\mathcal{E}_\ell\}, \quad (2)$$

where $k_\ell = 1/\ell$ is the ‘filtering wavenumber’ and $\{\cdot\}$ denotes a spatial average. Note that there is no factor of 2π in our definition of k_ℓ . Ref. 18 identified the conditions on the coarse-graining kernel for $\bar{E}(k_\ell, t)$ to be meaningful in the sense that its scaling agrees with that of the traditional Fourier spectrum when Fourier analysis is possible, such as in periodic domains. The Methods section shows how the filtering spectrum agrees with the Fourier spectrum performed within an oceanic box region over length-scales smaller than the box. The filtering spectrum has the important advantage of quantifying larger

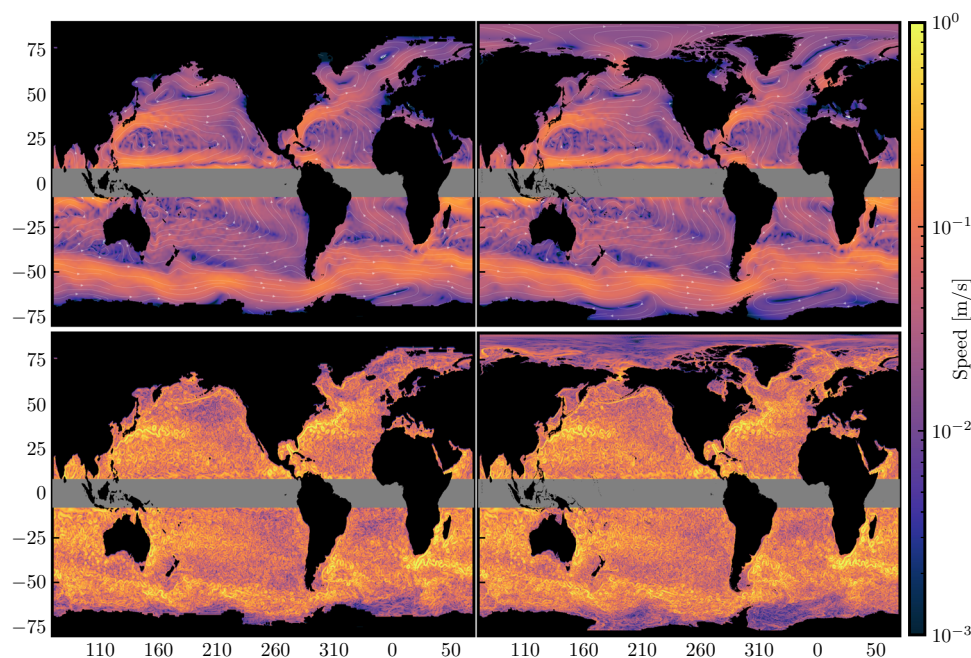


Fig. 1 | Gyre-scale and mesoscale flows. Colour maps show the geostrophic velocity magnitude for length scales [top] larger than 10^3 km and [bottom] smaller than 10^3 km for a single day (02 Jan 2015). [Left] shows the $1/4^\circ$ AVISO dataset and [right] the $1/12^\circ$ NEMO dataset. [White lines] highlight the corresponding

streamlines, with arrows showing the direction of the flow. Areas in black include land, and also ice coverage in the AVISO dataset. In this work, we exclude the tropics where velocity from satellite altimetry is less reliable, and define the northern and southern hemispheres (NH and SH, respectively) as the ocean poleward of 15° .

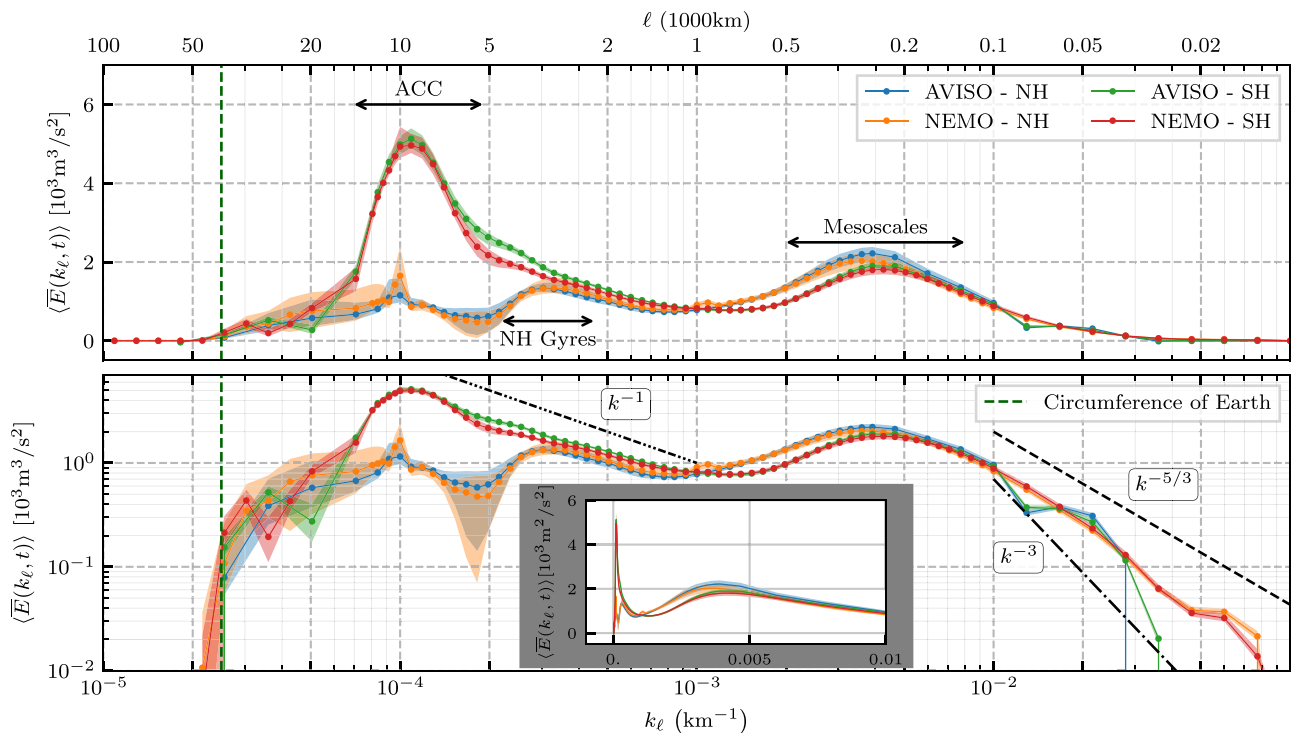


Fig. 2 | Power spectral density. Filtering wavenumber spectra (see Eq. (2)) of surface geostrophic KE for the global extratropical ocean from AVISO satellite altimetry and NEMO model re-analysis. Northern and southern hemispheres (NH and SH, respectively) extend poleward of 15°. The panels show the same data, but using [top] lin-log, [bottom] log-log, and [inset panel] lin-lin axes. Plots show the

temporal mean, $\langle \cdot \rangle$, of $\bar{E}(k_\ell, t)$ while envelopes show inter-quartile range (25th to 75th percentiles) of temporal variation. Data markers indicate length scales at which coarse-graining was performed. The vertical dashed green line at 4×10^4 km indicates the equatorial circumference of the Earth. Dashed black lines provide a reference for $-5/3$, -3 , and -1 power-law slopes in the bottom panel.

scales without being artificially limited by the box size and windowing functions, with such approaches used to synthetically periodize the data as required to use Fourier methods.

Figure 1 visualizes the flow from both AVISO satellite data and NEMO reanalysis model data (see “Methods”) from a single daily mean at scales larger than and smaller than 10^3 km, termed “gyre-scale” and “mesoscale”, respectively. The colour intensity illustrates the flow speed and is consistent with expectations that the large-scale flow magnitude is primarily dominated by the western boundary currents, while scales smaller than 10^3 km are dominated by mesoscale fluctuations. In the upper panels of Fig. 1, we can see clearly several well-known oceanic gyre structures, including the Beaufort Gyre in the Arctic, the Weddell and the Ross gyres in the Southern Ocean near Antarctica, the subtropical and subpolar gyres in the Atlantic and Pacific basins, and the ACC. North Atlantic currents are also readily observable, including the North Atlantic Current, its northward fork to the Norwegian Atlantic Current, and the southward East Greenland Current. The agreement between AVISO and NEMO is remarkable.

It is worth emphasizing that the flows in Fig. 1 are derived deterministically from a single daily mean of surface geostrophic velocity data without further temporal or statistical averaging. Past approaches have used climatological multi-year averaging (e.g., refs. 19,20) or Empirical Orthogonal Function (EOF) analysis (e.g., refs. 21,22), which is a statistical approach that requires averaging long time-series. Coarse-graining allows us to derive the dynamics governing the evolution of the flow in Fig. 1 (e.g., ref. 15), which is not possible for EOF analysis, and to disentangle length-scales and time-scales independently and in a self-consistent manner to study interactions between different spatio-temporal scales that link large-scale forcing, the mesoscale eddy field, and the global-scale circulation.

Results and discussion

Figure 2 shows the filtering spectrum for both the northern and southern hemispheres as obtained from Eq. (2) using surface geostrophic velocity data from both satellite altimetry and a high-resolution model (see “Methods”). This is the first spectrum showing the oceanic energy distribution across such a wide range of scales, from planetary scales $\mathcal{O}(10^4)$ km down to $\mathcal{O}(10)$ km.

The top and bottom panels in Fig. 2 plot the same spectrum in lin-log and log-log scale, respectively. The top panel highlights the prominent spectral peak due to the ACC, which is more than twice the mesoscale peak. The bottom panel highlights the power-law scaling over different k_ℓ bands. The inset in the bottom panel plots the same spectrum on a lin-lin scale and highlights the wide range of wavenumbers around 300 km.

Note the zero energy content at scales larger than Earth’s circumference and that energy also decreases precipitously when approaching the smallest scales resolved by each of the datasets, both of which are physical expectations. It is not possible for simulation, satellite, or field data to capture all scales present in the natural ocean, which certainly has scales smaller than 100 km. There is excellent agreement between satellite data and the higher resolution model data used here down to scales ≈ 100 km, which indicates that all scales larger than 100 km are well-resolved by both datasets, whereas smaller scales (10–100 km) are reasonably resolved only in the model data.

Antarctic circumpolar current and oceanic gyres

Unlike previously reported KE wavenumber spectra using Fourier analysis on box regions (e.g., refs. 6,8,9), some of which show a peak at mesoscales $\mathcal{O}(10^2)$ km, our Fig. 2 reveals that the largest spectral peak occurs at scales approximately 100 times larger, at $\approx 10^4$ km, and only in the southern hemisphere. Indeed, a circle of latitude at 50°S has a geodesic diameter of $\approx 8.9 \times 10^3$ km. This can also be seen from the

yellow colour of the ACC in Fig. 1 (top panels), highlighting its contribution to KE at large scales. Additional support that this spectral peak is due to the ACC can be found in Methods, where we plot the zonally (east-west) averaged KE as a function of latitude at various scales larger than 10^3 km. We can see that the dominant contribution is from latitudes [60°S, 40°S], which are roughly the latitudes of the ACC. We also see a much weaker signal at latitudes [30°N, 40°N], which roughly aligns with the Gulf Stream and Kuroshio. Further corroborating our assertion, the spectral peak in the southern hemisphere seen in Fig. 2 has no analogous peak in the northern hemisphere. Figure 2 shows vestiges of a similar peak in the northern hemisphere, but this is arrested at a smaller amplitude and at smaller scales ($\approx 4 \times 10^3$ km) due to continental boundaries.

Gyre-scale power law

The KE spectra from both hemispheres in Fig. 2 at scales larger than 10^3 km reveal a range of scales that exhibit a $\sim k^{-1}$ power-law. This scaling has been predicted by¹³ (see also ref. 14) for baroclinic modes at scales larger than the barotropic deformation radius, but has not been observed until now. The barotropic deformation radius is about 2×10^3 km in the oceans² and the ocean flow tends to be surface intensified as expected in a baroclinic flow²³. Thus, the k^{-1} scaling observed in Fig. 2 is consistent with¹³. Previous studies relying on Fourier analysis within box regions would have had difficulty detecting such scaling due to the box size artifacts. The k^{-1} extends to larger scales and peaks at scales $\approx 4 \times 10^3$ km in the north, which is broadly the scale at which the flow starts feeling continental boundaries and gyres form. This can also be seen from the bright yellow colour of the Gulf Stream and Kuroshio in Fig. 1, highlighting their contribution to KE at large scales. In the southern hemisphere, on the other hand, the k^{-1} scaling extends up to the scale of the ACC, which encounters no continental barriers (at the latitudes of the Drake Passage) as it flows eastward around Antarctica.

Mesoscale eddies

In Fig. 2, we find a second spectral peak between 100 and 500 km, centred at $\ell \approx 300$ km, that is associated with the mesoscale flow. While we can see from Fig. 2 that the mesoscales do not form the largest peak of the KE spectrum, their cumulative contribution between scales 100 and 500 km greatly exceeds that of scales larger than 10^3 km. This is because the mesoscale flow populates a wider range of wavenumbers compared to the gyre-scale flow (note the logarithmic x -axis and the inset on a linear x -axis). Indeed, integrating the energy spectrum in Fig. 2 within the band 100–500 km yields more than $\approx 50\%$ of the total energy resolved by either satellites or the mesoscale eddying model in the extratropics. Coarse-graining allows us to determine this fraction of KE belonging to the mesoscales in the global ocean. This is because integrating the filtering spectrum over all k_ℓ in Fig. 2 yields the total KE (as resolved by the data), which was not possible in past studies using Fourier analysis in regional boxes.

The power-law spectral scaling at mesoscales and smaller scales has been the focus of many previous studies (e.g., refs. 6,11,24,25) using Fourier analysis within box regions. While this is not our focus here, we observe that the overall mesoscale spectral scaling lies between $k^{-5/3}$ and k^{-3} in Fig. 2, consistent with previous studies^{24,26}. Note that mesoscale power-law scaling is more clearly seen in smaller regions (see Methods) as the mesoscale power-law and the corresponding wavenumber range change significantly depending on the geographical location (see Fig. 15 of ref. 11).

Characteristic velocity and energy content within key scale bands

From the spectra in Fig. 2, we partition the energy conservatively into four bands of interest: $\ell \leq 100$ km, 100–500 km, 500– 10^3 km, and $\ell \geq 10^3$ km such that the sum of their energy equals total KE resolved in the data. From KE within a scale band, KE_{band} , we can infer a

Table 1 | Energy content of scale ranges

ℓ -band	1/12° NEMO			
	RMS Vel. [cm/s]		% of total KE	
	NH	SH	NH	SH
$\ell \leq 100$ km	13.15	13.29	37.8	39.7
100–500 km	15.48	15.00	53.2	50.2
500–1000 km	4.64	4.08	4.7	3.7
$1000 \text{ km} \leq \ell$	4.26	5.31	4.0	6.2
1/4° AVISO				
$\ell \leq 100$ km	11.21	11.24	28.9	30.8
100–500 km	16.32	15.36	61.9	57.7
500–1000 km	4.57	4.05	4.9	4.0
$1000 \text{ km} \leq \ell$	4.16	5.53	4.0	7.4

The RMS velocity in separate ℓ bands for each hemisphere, as well as the percent of total KE contained within each ℓ band, for both the [upper half] 1/12° NEMO and [lower half] 1/4° AVISO datasets. See Table 2 in “Methods” for uncertainty estimates.

characteristic root-mean-square (RMS) velocity, $u_{\text{rms}} = \sqrt{2 \times KE_{\text{band}}}$ at those scales. The results are summarized in Table 1. The mesoscale band (100–500 km) has the highest RMS velocity, between 15 and 16 cm/s, and accounts for more than 50% of the total energy resolved in the data. Mesoscales are slightly more energetic (per unit area) in the NH than SH. There have been several past attempts to quantify the mesoscale fraction of total oceanic KE, which is often cited as being 80%²⁷. However, such estimates have large uncertainties due to working in small representative box regions that do not cover the global ocean²⁸ or due to relying on subjective detection criteria for mesoscale eddies³ or on a Reynolds (or temporal) decomposition of the flow¹. Table 1 shows that all resolved scales smaller than 500 km constitute $\approx 90\%$ of the total surface geostrophic KE in the global extratropical ocean.

Table 1 allows us to also infer a characteristic advective timescale, $\tau_{\text{meso}} = \ell / u_{\text{rms}} = \mathcal{O}(25)$ days. The RMS velocity decreases significantly for larger scales, with hemisphere-asymmetries becoming more prominent. Within the ACC-containing band of $\ell > 10^3$ km, the NH and SH RMS velocities are approximately 4.2 and 5.4 cm/s, respectively, and with an associated characteristic timescale $\tau_{\text{gyre}} = \ell / u_{\text{rms}} = \mathcal{O}(\text{few})$ years.

Seasonality and spectral lag time

Figure 3 shows the seasonality in surface KE as a function of length-scale from both satellite and model data, which exhibit similar trends. The most striking feature of Fig. 3 is the approximately constant lag time between length-scales of the same ratio as they attain seasonal maxima (red) and minima (blue). Going from 10 km up to 10^3 km, length-scales that are $\times 2$ larger experience a lag of ≈ 40 days in their seasonal cycle, such that in both hemispheres KE at 100 km peaks in spring while KE at 10^3 km peaks in late summer. Figure 3 plots the normalized deviation, or z-score, $z(t) = (x(t) - \mu) / \sigma$, where μ and σ are the temporal mean and standard deviation of the spectrum $x = \bar{E}(t)$ at each scale k_ℓ . A detailed regression analysis is in the Methods section. These results agree with and extend previous analysis within regional boxes^{24,29,30}, which found that scales between 50 and 100 km have maximal KE in the spring while scales larger than 200 km (but smaller than the box) tend to peak with a delay of one to two months. Possible explanations for the seasonal variation in KE at different scales include the increased eddy-killing from winter’s high winds¹⁷, and an inverse energy cascade from the submesoscales which energizes mesoscales in spring months^{24,30}. While Fig. 3 is suggestive of an inverse cascade, in which seasonal variations propagate up-scale at the rate we observe, it alone is not sufficient evidence (see ref. 31 for other possible causes) and a direct measurement of the cascade as in ref. 15 is required but is beyond our scope here.

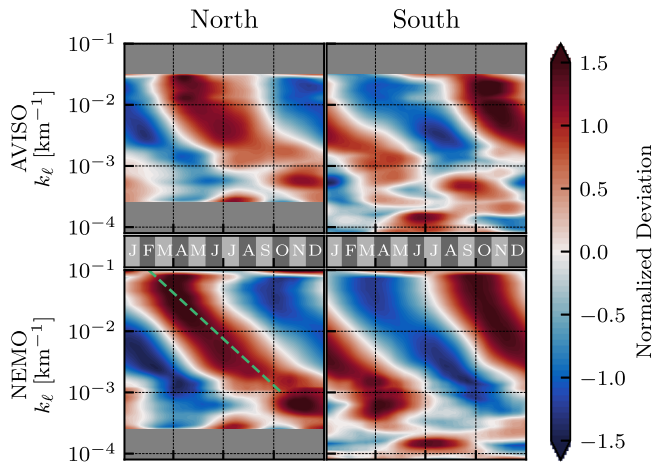


Fig. 3 | Seasonality. Normalized deviation (or z-score) of the 60-day running average of surface geostrophic KE spectrum in [left] NH and [right] SH for both [top] satellite and [bottom] model datasets. Horizontal axis shows time binned into months, from January (J) through December (D). Vertical axes show filtering wavenumber $k_\ell = \ell^{-1}$. The green line in the bottom left panel shows a 100-fold scale increase over 8 months.

Gyre-scales. At gyre-scales the surface flow is influenced directly by continental boundaries, wind, and buoyancy forcing. Indeed, at scales $> 10^3$ km in Fig. 3, there is a noticeable break in the seasonal trends we discussed in the previous paragraph. In the SH, where the ACC is not impeded by continents, we see from Fig. 3 a pronounced winter peak at $\approx 10 \times 10^3$ km, which correlates with maximal wind forcing¹⁷. Scales between 10^3 km and 3×10^3 km in both hemispheres peak in autumn, consistent with previous analysis showing an autumn maximum in the surface flow of western boundary currents^{32–34} due to the upper ocean seasonal heating cycle. At NH scales larger than 5×10^3 km, the KE is too small to be meaningful (Fig. 2).

Outlook

Using both satellite and model ocean data, our coarse-graining characterization of surface geostrophic velocity revealed novel spectral features, including the ACC and basin-scale gyres. By partitioning kinetic energy across length-scales in a manner that conserves energy and covers the global ocean, we showed that length-scales $\ell < 500$ km make an overwhelming contribution to surface geostrophic kinetic energy due to populating a wide range of wavenumbers, despite not forming the most prominent spectral peak. Based on prior characterizations of ocean energy¹, we reason that these length scales are dominated by mesoscale features such as geostrophic turbulence, boundary currents, and fronts. Our analysis also revealed a characteristic lag time, with length-scales that are twice as large experiencing a lag of ≈ 40 days in their seasonal cycle.

The expanded spectral analysis spurs new questions and lines of inquiry. We hope future investigations will shed light on the dynamic coupling between the spectral peaks at the gyre scales and mesoscales, determine if the k^{-3} slope between the two peaks is indeed due to baroclinic modes^{13,14}, and whether the characteristic spectral lag-time is caused by an inverse cascade.

Methods

Description of datasets

For the geostrophic ocean surface currents, we use a Level 4 (L4) post-processed dataset of daily-averaged geostrophic velocity on a $1/4^\circ$ grid spanning January 2010 to October 2018 (except for the seasonality analysis, where we use 2012–2016). The data is obtained from the AVISO + analysis of multi-mission satellite altimetry measurements for sea surface height (SSH)³⁵. The product identifier of the AVISO dataset

used in this work is “SEALEVEL_GLO_PHY_L4_MY_008_047” (<https://doi.org/10.48670/moi-00148>).

We also analyze 1-day averaged surface SSH-derived currents from the NEMO numerical modelling framework, which is coupled to the Met Office Unified Model atmosphere component, and the Los Alamos sea ice model (CICE). The NEMO dataset consists of weakly coupled ocean-atmosphere data assimilation and forecast system, which is used to provide 10 days of 3D global ocean forecasts on a $1/12^\circ$ grid. We use daily-averaged data that spans four years, from 2015 to 2018. More details about the coupled data assimilation system used for the production of the NEMO dataset can be found in refs. 36,37. The specific product identifier of the NEMO dataset used here is “GLOBAL_MULTIYEAR_PHY_001_030” (<https://doi.org/10.48670/moi-00021>).

Coarse-graining on the sphere

For a field $\phi(\mathbf{x})$, a “coarse-grained” or (low-pass) filtered field, which contains only length-scales larger than ℓ , is defined as

$$\bar{\phi}_\ell(\mathbf{x}) = G_\ell * \phi, \tag{3}$$

where $*$, in the context of this work, is a convolution on the sphere as shown in ref. 16 and $G_\ell(\mathbf{r})$ is a normalized kernel (or window function) so that $\int d^2\mathbf{r} G_\ell(\mathbf{r}) = 1$. Operation (3) may be interpreted as a local space average over a region of diameter ℓ centred at point \mathbf{x} . The kernel G_ℓ that we use here is essentially a graded top-hat kernel:

$$G_\ell(\mathbf{x}) = \frac{A}{2} \left(1 - \tanh \left(10 \left(\frac{\gamma(\mathbf{x})}{\ell/2} - 1 \right) \right) \right). \tag{4}$$

We use geodesic distance, $\gamma(\mathbf{x})$, between any location $\mathbf{x} = (\lambda, \phi)$ on Earth’s surface relative to location (λ_0, ϕ_0) where coarse-graining is being performed, which we calculate using

$$\gamma(\mathbf{x}) = R_E \arccos [\sin(\phi) \sin(\phi_0) + \cos(\phi) \cos(\phi_0) \cos(\lambda - \lambda_0)], \tag{5}$$

with $R_E = 6371$ km for Earth’s radius. In Eq. (4), A is a normalization factor, evaluated numerically, to ensure G_ℓ area integrates to unity. A convolution with G_ℓ in Eq. (4) is a spatial analogue to an ℓ -day running time-average.

The above formalism holds for coarse-graining scalar fields. To coarse-grain a vector field on a sphere generally requires more care¹⁶, particularly for vector fields that need not be toroidal (2D non-divergent). However, as this work focuses on SSH-derived 2D non-divergent velocity fields, these concerns do not apply here. More details can be found in ref. 38.

Comparing coarse-graining to Fourier analysis. It is common to quantify the spectral distribution of ocean kinetic energy via Fourier transforms computed either along transects or within regions; e.g., refs. 10,12,39–42. This approach has rendered great insights into the length scales of oceanic motion and the cascade of energy through these scales^{43–47}. However, it has notable limitations for the ocean where the spatial domain is generally not periodic, thus necessitating adjustments to the data (e.g., by tapering) before applying Fourier transforms. Methods to produce an artificially periodic dataset can introduce spurious gradients, length-scales, and flow features not present in the original data¹⁸. A related limitation concerns the chosen region size, with this size introducing an artificial upper length scale cutoff along with an artificial discreteness of wavenumbers that can bias the KE distribution across scales. In this manner, no scales are included that are larger than the region size even if larger structures exist in the ocean. Furthermore, the data is typically assumed to lie on a flat tangent plane to enable the use of Cartesian coordinates. However, if the region becomes large enough to sample the earth’s curvature,

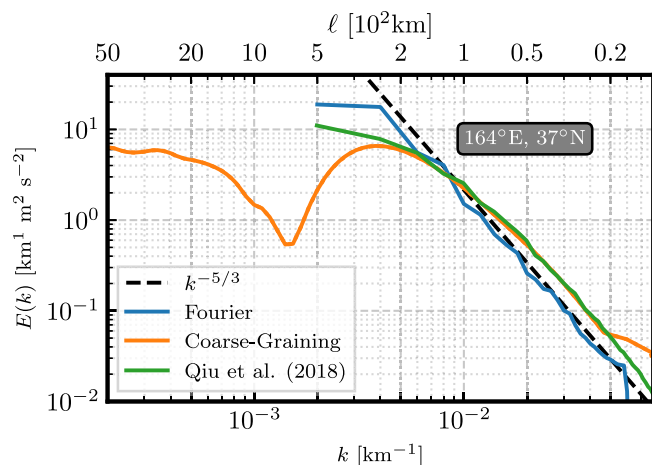


Fig. 4 | Energy spectra. Comparison of the filtering spectrum (orange), traditional Fourier spectrum (blue), and the Fourier spectrum from ref. 6 (green, data kindly provided by authors of ref. 6) for the $5^\circ \times 5^\circ$ box region centred at 164°E , 37°N (roughly the Kuroshio extension). The dashed black line provides a reference for a $-5/3$ slope. Note that the ℓ axis (top) is in 100 km.

then that puts into question the use of the familiar Cartesian Fourier analysis of sines and cosines. The use of spherical harmonics, common for the atmosphere, is not naturally suitable for the ocean, again since the ocean boundaries are irregular. These limitations mean that in practice, Fourier methods are only suited for open ocean regions away from boundaries, and over a rather limited regional size.

As a demonstration of both the validity and advantages of coarse-graining for energy spectra, consider Fig. 4. This figure reproduces the energy spectrum from Fig. 3 of ref. 6, and includes both the coarse-graining, and traditional Fourier energy spectra measured from the $1/12^\circ$ NEMO dataset. Spectra are calculated for the $5^\circ \times 5^\circ$ box centred at 164°E , 37°N , which corresponds to the Kuroshio extension.

For length scales $\lesssim 200$ km, the three spectra generally agree very well, and all produce close to a $-5/3$ spectrum. Ref. 6 used a higher resolution dataset, and so the spectra disagree for scales < 20 km as expected. At larger scales, coarse-graining does not require tapering, and so the spectrum at scales ≥ 200 km is not contaminated by the shape of the tapering window or the box size. As a result, coarse-graining is able to detect that the spectrum for this region peaks at ≈ 250 km. An exact relation between Fourier wavenumbers k and filtering wavenumbers k_ℓ is provided by eq. (16) in ref. 18, which shows that the filtering spectrum $\bar{E}(k_\ell)$ at k_ℓ is essentially a weighted average of the traditional Fourier spectrum $E(k)$ over a range of Fourier wavenumbers k centred around k_ℓ . Therefore, it is worth being mindful that agreement between filtering and Fourier spectra may not be perfect in practice, as discussed at length in¹⁸, due to the fact that compact spatial filtering kernels are not strictly local in k -space compared to a sharp-spectral filter, which can lead to additional smoothing as a function of scale. This is the price paid for gaining spatially local information, such as allowing us to distinguish the tropics and the hemispheres (see also Figs. 1 and 5), since concurrently exact spatial and scale localization is forbidden by the uncertainty principle.

ACC as the spectral peak. In Fig. 5 we provide plots a visualization of the zonally-averaged kinetic energy for selected filtering scales. Scales larger than 10^3 km have a dominant contribution from latitudes $[60^\circ\text{S}, 40^\circ\text{S}]$, roughly corresponding to the ACC, and another contribution over $[30^\circ\text{N}, 40^\circ\text{N}]$, roughly corresponding to the NH western boundary currents. Scales larger than 5×10^3 km continue to show a clear ACC signal, with no NH signal since this filter scale is just beyond the NH gyre spectral peak. Finally, scales larger than 12×10^3 km have no distinct ACC signal, showing that the ACC has been fully removed by

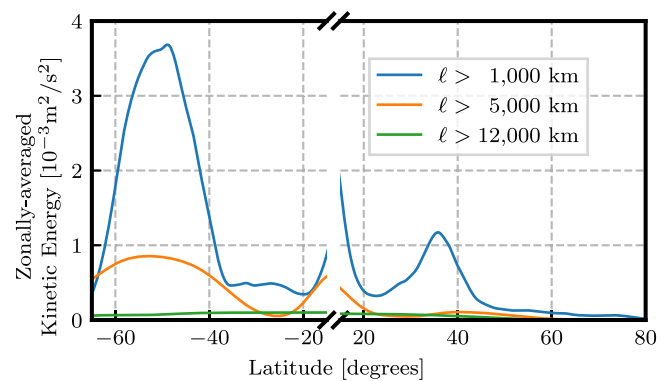


Fig. 5 | Energy by latitude. Time- and zonally-averaged kinetic energy computed from AVISO as a function of latitude for a selection of filter scales (see legend). Note that the latitude axis is broken to exclude the band $[15^\circ\text{S}, 15^\circ\text{N}]$.

coarse-graining at this scale. Combined, these results provide further support for our claim that the 10^4 km spectral peak corresponds to the ACC.

Land treatment. When coarse-graining near land, it is necessary to have a methodology for incorporating land into the filtering kernel (c.f. ref. 38 for more in-depth discussion of land treatments). In the work presented here, we make the choice of treating land as zero velocity water. Since coarse-graining is essentially a ‘blurring’ (analogized with taking off one’s glasses to have a blurrier picture), the land-water division itself also become less well-defined, and so treating land as zero-velocity water is both conceptually consistent and aligns with no-flow boundary conditions. Additionally, this land treatment allows for a ‘fixed’ (or homogeneous) filtering kernel at all points in space, and as a result allows for commutativity with derivatives (e.g., divergence-free flows remain divergence-free after coarse-graining)¹⁶. Note, however, that only the true water area is used as the denominator when computing area averages (e.g., the NH area-averaged energy is the coarse KE summed over *all* NH cells, including land, divided by the *water-area* of NH). This is merely a normalization choice and does not affect our results. For NEMO data, the normalization area is 104×10^6 km² in NH and 155×10^6 km² in SH. For AVISO, the area varies with time due to sea ice coverage, between $[90.5, 98.7] \times 10^6$ km² for NH and $[141, 154] \times 10^6$ km² for SH.

Deforming kernel approach. An alternative choice is to *deform* the kernel around land, so that only water cells are included, at the cost of losing the homogeneity of the kernel. The benefit to this approach is that it does not require conceptually treating land as zero velocity water. However, it has the significant drawback that coarse-graining no longer commutes with differentiation and, as a result, does not necessarily preserve flow properties such as being divergence-free. Additionally, a kernel that is inhomogeneous (i.e., changes shape depending on geographic location) does not necessarily conserve domain averages, including the kinetic energy of the flow, and has the potential to both increase or decrease the domain average. More details are provided in ref. 38.

Comparing land treatments. Figure 6 presents the energy spectra, similar to Fig. 2 in the main text, using both deforming and fixed kernels for the single day 02 Jan 2015. The deforming-kernel spectra agree remarkably well with the non-deforming (fixed) kernel spectra, in that they present the mesoscales, ACC, and gyre peaks at similar scales. There are some quantitative differences, such as the deforming kernel SH spectra presents a slightly broader and higher-magnitude ACC peak.

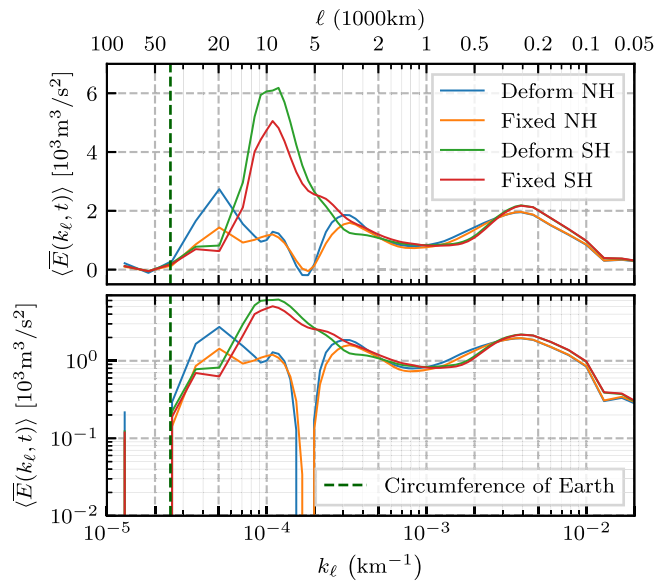


Fig. 6 | Land treatments. Filtering spectra, analogous to Fig. 2, using both deforming and fixed kernels on the AVISO dataset for a single day (02 Jan 2015).

Isolating hemisphere spectra. In this work, we are primarily concerned with the extra-tropical latitudes: [90°S, 15°S] and [15°N, 90°N]. However, at very large length scales information from the equatorial band and opposing hemisphere can become introduced through the filter kernel. To resolve this issue, we use a ‘reflected hemispheres’ approach, wherein one hemisphere is reflected and copied onto the other hemisphere, essentially producing a world with two north, or two south hemispheres. It is worth noting that reflected hemispheres and equatorial masking would not be necessary in a context where ageostrophic velocities are also considered and a global power spectrum is desired. They are used here because we wish to disentangle the power spectra of the geostrophic flow in each of the extra-tropical hemispheres.

Figure S2 in the Supplementary Material (SM) shows the filtering spectra from NEMO without relying on hemisphere reflection, and is to be compared to Fig. 2 in the main text. The two are in qualitative agreement, with an ACC peak in the SH and mesoscale peaks in both hemispheres. Unsurprisingly, the spectra only deviate for very large filtering scales, where an increasing amount of extra-hemisphere information is captured by the large kernels. Specifically, the NH spectra has a third peak at scales $\ell > 10^4$ km that is not present when using reflected hemispheres. This very large-scale peak is a result of the NH kernels capturing the ACC. It is worth noting, however, that the main ACC peak is still present in the SH spectra, as is the NH gyre peak at approximately $\ell = 3 \times 10^3$ km.

Uncertainty estimates of ℓ -band values

Table 1 presented median values of the RMS velocity and percentage of total KE contained within various ℓ -bands. Table 2 presents the interquartile range (25th to 75th percentiles) to provide an estimate for the sensitivity of those values.

Seasonality

A 60-day running mean is applied to remove higher frequencies and allow us to better consider the longer-time trend, and individual years are averaged onto a ‘typical’ year for the purpose of comparison. Seasonality results use the 5 years spanning 2012–2016 for AVISO, and the 4 years spanning 2015–2018 for NEMO.

A useful statistical method for comparing signals is to compare the normalized deviations, or z-scores, of the signal. For a set of points

Table 2 | Energy content of scale ranges

ℓ -band	1/12° NEMO			
	RMS Vel. [cm/s]		% of total KE	
	NH	SH	NH	SH
$\ell \leq 100$ km	12.77–13.56	12.98–13.78	36.3–40.5	38.2–41.0
100–500 km	14.97–16.16	14.57–15.46	50.8–54.6	49.0–51.5
500–1000 km	4.47–4.79	3.99–4.16	4.3–5.1	3.4–3.9
1000 km $\leq \ell$	4.11–4.43	5.27–5.36	3.6–4.4	5.9–6.6
1/4° AVISO				
$\ell \leq 100$ km	10.89–11.55	11.04–11.57	28.3–30.2	30.1–31.7
100–500 km	15.62–16.83	15.02–15.79	60.7–62.8	56.7–58.5
500–1000 km	4.46–4.68	3.98–4.12	4.6–5.2	3.8–4.2
1000 km $\leq \ell$	4.06–4.26	5.47–5.57	3.7–4.4	7.0–7.7

Interquartile range of RMS velocity values (left half) and percent of total kinetic energy in separate ℓ bands in each hemisphere, for both the [upper half] 1/12° NEMO and [lower half] 1/4° AVISO datasets.

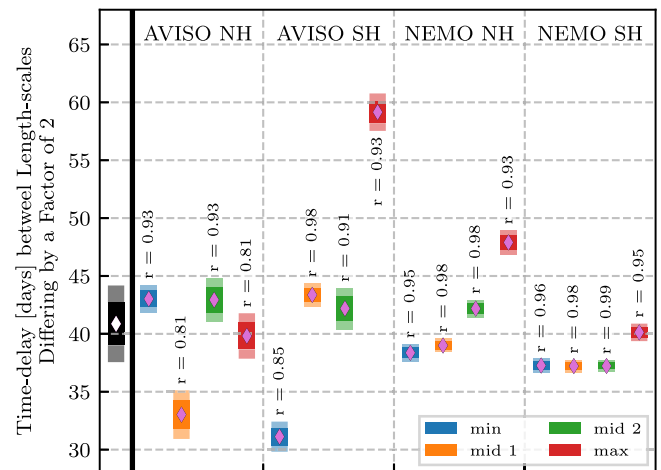


Fig. 7 | Regression analysis summary. Regression slope estimates and confidence intervals for each of the datasets shown in Fig. S3. Vertical dashed lines separate the data sources, with the text along the top indicating the source data and hemisphere. Diamonds indicate the regression slope estimate, dark envelopes the 75% confidence interval, and light envelopes the 95% confidence interval. The r -value for each regression fit is printed alongside the corresponding slope distribution. The left-most illustration, separated by a thick black line, presents the mean (diamond) and confident intervals (envelopes) across the 16 regression analyses. In the legend, ‘min’ means the lowest 10% z-score, ‘mid’ the two middle-most 10% groups, and ‘max’ the highest 10%.

$\{x_i | i = 1 \dots N\}$, each point x_i is transformed into a corresponding z-score z_i via $z_i = (x_i - \mu_x) / \sigma_x$, where μ_x and σ_x are the mean and standard deviation of the x_i . As a result, data points that are larger than the mean produce a positive z-score, while those smaller than the mean produce a negative z-score. Note that the normalized deviation (z-scores) in Fig. 3 are computed independently for each k_ℓ , and so comparing magnitudes between scales is non-trivial.

Regression analysis of phase shift. Figure 3 presents a clear phase shift in the seasonal cycle as a function of length-scale. In order to quantify the phase shift, we need to first extract a meaningful set of (k_ℓ, time) points. To that end, we extract, for each k_ℓ , the (i) times corresponding to the lowest 10% (dark blue in Fig. 3), (ii) two middle-most 10% for the two zero-crossings (white in Fig. 3), and (iii) highest 10% (dark red in Fig. 3) of the normalized deviations presented in Fig. 3. This is essentially extracting the (k_ℓ, time) -coordinates for the line of

darkest red, darkest blue, and the two white lines, resulting in a total of four regression sets. Periodic phase adjustment to the days of the year is applied to maintain monotonicity in time, and the k_r grid is truncated to focus on regimes with a clear linear trend. The extracted data points are shown as the dots/vertical bars in Fig. S3 in the SM, along with their corresponding regression fits.

Figure 7 presents the linear regression slope analysis for the data shown in Fig. S3. The different regression analyses generally agree well, with 12 of the 16 regression sets indicating a 35–45 day time-lag per octave of spatial scales. From this analysis, we conclude that length-scales that differ by a factor of two (i.e., $\ell_1/\ell_2 = 2$) have seasonal cycles that are off-set by 41 ± 3 days. Scales that differ a decade ($\ell_1/\ell_2 = 10$) would correspondingly have a phase shift of 136 ± 10 days, or roughly 4.5 months.

Data availability

All data needed to evaluate or reproduce the results in the paper are present either in the paper or is publicly available. Data underlying our analysis can be downloaded from CMEMS at <https://marine.copernicus.eu/services-portfolio/access-to-products/>.

Code availability

The coarse-graining analysis was performed using our code FlowSieve, which is publicly available at <https://github.com/husseinaluie/FlowSieve>.

References

- Ferrari, R. & Wunsch, C. Ocean circulation kinetic energy: Reservoirs, sources, and sinks. *Annu. Rev. Fluid Mech.* **41**, 253–282 (2009).
- Vallis, G. K. *Atmospheric and Oceanic Fluid Dynamics* 2nd edn (Cambridge University Press, 2017).
- Chelton, D. B., Schlax, M. G. & Samelson, R. M. Global observations of nonlinear mesoscale eddies. *Prog. Oceanogr.* **91**, 167–216 (2011).
- Klein, P. et al. Ocean-scale interactions from space. *Earth Space Sci.* **6**, 795–817 (2019).
- Menemenlis, D., Hill, C., Henze, C. E., Wang, J. & Fenty, I. Southern Ocean Pre-SWOT Level-4 Hourly MITgcm LLC4320 Native Grid 2km Oceanographic Dataset Version 1.0. Ver. 1.0. Dataset accessed at <https://doi.org/10.5067/PRESW-ASJ10> (PO.DAAC, CA, USA, 2021).
- Qiu, B. et al. Seasonality in transition scale from balanced to unbalanced motions in the world ocean. *J. Phys. Oceanogr.* **48**, 591–605 (2018).
- Marshall, J., Scott, J. R., Romanou, A., Kelley, M. & Leboissetier, A. The dependence of the ocean's moc on mesoscale eddy diffusivities: A model study. *Ocean Modelling* **111**, 1–8 (2017).
- Sasaki, H., Klein, P., Qiu, B. & Sasai, Y. Impact of oceanic-scale interactions on the seasonal modulation of ocean dynamics by the atmosphere. *Nat. Commun.* **5**, 1–8 (2014).
- Torres, H. S. et al. Partitioning ocean motions into balanced motions and internal gravity waves: A modeling study in anticipation of future space missions. *J. Geophys. Res.-Oceans* **123**, 8084–8105 (2018).
- O'Rourke, A. K., Arbic, B. K. & Griffies, S. M. Frequency-domain analysis of atmospherically forced versus intrinsic ocean surface kinetic energy variability in GFDL's CM2-O model hierarchy. *J. Clim.* **31**, 1789–1810 (2018).
- Stammer, D. Global characteristics of ocean variability estimated from regional TOPEX/POSEIDON altimeter measurements. *J. Phys. Oceanogr.* **27**, 1743–1769 (1997).
- Callies, J. & Wu, W. Some expectations for submesoscale sea surface height variance spectra. *J. Phys. Oceanogr.* **49**, 2271–2289 (2019).
- Müller, P. & Frankignoul, C. Direct atmospheric forcing of geostrophic eddies. *J. Phys. Oceanogr.* **11**, 287–308 (1981).
- Wortham, C. & Wunsch, C. A multidimensional spectral description of ocean variability. *J. Phys. Oceanogr.* **44**, 944–966 (2014).
- Aluie, H., Hecht, M. & Vallis, G. K. Mapping the energy cascade in the north atlantic ocean: The coarse-graining approach. *J. Phys. Oceanogr.* **48**, 225–244 (2018).
- Aluie, H. Convolutions on the sphere: Commutation with differential operators. *GEM-Int. J. Geomath.* **10**, 9 (2019).
- Rai, S., Hecht, M., Maltrud, M. & Aluie, H. Scale of oceanic eddy killing by wind from global satellite observations. *Science Advances* **7**, eabf4920 (2021).
- Sadek, M. & Aluie, H. Extracting the spectrum of a flow by spatial filtering. *Phys. Rev. Fluids* **3**, 124610 (2018).
- Aguiar-González, B. et al. Seasonal variation of the south indian tropical gyre. *Deep Sea Res. Part I: Oceanogr. Res. Papers* **110**, 123–140 (2016).
- Shi, J.-R., Talley, L. D., Xie, S.-P., Peng, Q. & Liu, W. Ocean warming and accelerating southern ocean zonal flow. *Nat. Clim. Change* **11**, 1090–1097 (2021).
- Trenberth, K. E. A quasi-biennial standing wave in the southern hemisphere and interrelations with sea surface temperature. *Q. J. R. Meteorol. Soc.* **101**, 55–74 (1975).
- Di Lorenzo, E. et al. North Pacific Gyre Oscillation links ocean climate and ecosystem change. *Geophys. Res. Lett.* **35**, L08607 (2008).
- Wunsch, C. The vertical partition of oceanic horizontal kinetic energy. *J. Phys. Oceanogr.* **27**, 1770–1794 (1997).
- Uchida, T., Abernathey, R. & Smith, S. Seasonality of eddy kinetic energy in an eddy permitting global climate model. *Ocean Modelling* **118**, 41–58 (2017).
- Khatri, H., Griffies, S. M., Uchida, T., Wang, H. & Menemenlis, D. Role of mixed-layer instabilities in the seasonal evolution of eddy kinetic energy spectra in a global submesoscale permitting simulation. *Geophys. Res. Lett.* **48**, 1–13 (2021).
- Xu, Y. & Fu, L. L. The effects of altimeter instrument noise on the estimation of the wavenumber spectrum of sea surface height. *J. Phys. Oceanogr.* **42**, 2229–2233 (2012).
- Klein, P. et al. Ocean-scale interactions from space. *Earth Space Sci.* **6**, 795–817 (2019).
- Wunsch, C. The oceanic variability spectrum and transport trends. *Atmosphere-Ocean* **47**, 281–291 (2009).
- Qiu, B., Chen, S., Klein, P., Sasaki, H. & Sasai, Y. Seasonal mesoscale and submesoscale eddy variability along the North Pacific subtropical countercurrent. *J. Phys. Oceanogr.* **44**, 3079–3098 (2014).
- Sasaki, H., Klein, P., Sasai, Y. & Qiu, B. Regionality and seasonality of submesoscale and mesoscale turbulence in the north pacific ocean. *Ocean Dyn.* **67**, 1195–1216 (2017).
- Zhao, D., Betti, R. & Aluie, H. Scale interactions and anisotropy in Rayleigh-Taylor turbulence. *J. Fluid Mech.* **930**, 1–40 (2022).
- Wang, L. & Koblinsky, C. J. Low-frequency variability in regions of the Kuroshio extension and the gulf stream. *J. Geophys. Res.: Oceans* **100**, 18313–18331 (1995).
- Wang, L. & Koblinsky, C. J. Low-frequency variability in the region of the Agulhas retroflection. *J. Geophys. Res.: Oceans* **101**, 3597–3614 (1996).
- Kelly, K. A., Singh, S. & Huang, R. X. Seasonal variations of sea surface height in the gulf stream region. *J. Phys. Oceanogr.* **29**, 313–327 (1999).
- Pujol, M.-I. et al. Duacs dt2014: The new multi-mission altimeter data set reprocessed over 20 years. *Ocean Sci.* **12**, 1067–1090 (2016).
- Hewitt, H. T. et al. Design and implementation of the infrastructure of hadgem3: The next-generation met office climate modelling system. *Geosci. Model Dev.* **4**, 223–253 (2011).
- Lea, D. et al. Assessing a new coupled data assimilation system based on the met office coupled atmosphere–land–ocean–sea ice model. *Monthly Weather Rev.* **143**, 4678–4694 (2015).

38. Buzziotti, M., Storer, B. A., Griffies, S. M. & Aluie, H. A coarse-grained decomposition of surface geostrophic kinetic energy in the global ocean. *Earth Space Sci. Open Archive* <https://doi.org/10.1002/essoar.10507290.1> (2021).
39. Fu, L.-L. & Smith, R. D. Global ocean circulation from satellite altimetry and high-resolution computer simulation. *Bull. Am. Meteorol. Soc.* **77**, 2625–2636 (1996).
40. Chen, R., Gille, S. T., McClean, J. L., Flierl, G. R. & Griesel, A. A multiwavenumber theory for eddy diffusivities and its application to the Southeast Pacific (DIMES) region. *J. Phys. Oceanogr.* **45**, 1877–1896 (2015).
41. Rocha, C. B., Chereskin, T. K., Gille, S. T. & Menemenlis, D. Mesoscale to submesoscale wavenumber spectra in Drake passage. *J. Phys. Oceanogr.* **46**, 601–620 (2016).
42. Khatri, H., Sukhatme, J., Kumar, A. & Verma, M. K. Surface ocean enstrophy, kinetic energy fluxes, and spectra from satellite altimetry. *J. Geophys. Res.: Oceans* **123**, 3875–3892 (2018).
43. Scott, R. B. & Wang, F. Direct evidence of an oceanic inverse kinetic energy cascade from satellite altimetry. *J. Phys. Oceanogr.* **35**, 1650 (2005).
44. Scott, R. B. & Arbic, B. K. Spectral energy fluxes in geostrophic turbulence: Implications for ocean energetics. *J. Phys. Oceanogr.* **37**, 673–688 (2007).
45. Arbic, B. K. et al. Nonlinear cascades of surface oceanic geostrophic kinetic energy in the frequency domain. *J. Phys. Oceanogr.* **42**, 1577–1600 (2012).
46. Arbic, B. K., Polzin, K. L., Scott, R. B., Richman, J. G. & Shriver, J. F. On eddy viscosity, energy cascades, and the horizontal resolution of gridded satellite altimeter products*. *J. Phys. Oceanogr.* **43**, 283–300 (2013).
47. Arbic, B. K. et al. Geostrophic turbulence in the frequency–wavenumber domain: Eddy-driven low-frequency variability. *J. Phys. Oceanogr.* **44**, 2050–2069 (2014).

Acknowledgements

We thank D. Balwada, M. Jansen, S. Rai, and B. Reichl for valuable discussions and comments. We also thank B. Qiu for kindly sharing the data used in Fig. 4. This research was funded by US NASA grant 8ONSSC18K0772 and NSF grant OCE-2123496. H.A. was also supported by US DOE grants DE-SC0014318, DE-SC0020229, DE-SC0019329, NSF grants PHY-2020249, PHY-2206380, and US NNSA grants DE-NA0003856, DE-NA0003914. H.K. acknowledges the support from UK NERC grant NE/T013494/1. Computing time was provided by NERSC under Contract No. DE-AC02-05CH11231 and NASA's HEC Programme through NCCS at Goddard Space Flight Centre. This work was also

supported by the European Research Council (ERC) under the European Union's Horizon 2020 research and innovation programme (Grant Agreement No. 882340).

Author contributions

B.S. carried out most of the data analysis with some assistance from M.B. H.A. conceived of the initial idea. B.S., M.B., H.K., S.G., and H.A. contributed to the interpretation of the results and writing of the manuscript.

Competing interests

The authors declare no competing interests.

Additional information

Supplementary information The online version contains supplementary material available at

<https://doi.org/10.1038/s41467-022-33031-3>.

Correspondence and requests for materials should be addressed to Hussein Aluie.

Peer review information *Nature Communications* thanks the anonymous reviewer(s) for their contribution to the peer review of this work.

Reprints and permission information is available at <http://www.nature.com/reprints>

Publisher's note Springer Nature remains neutral with regard to jurisdictional claims in published maps and institutional affiliations.

Open Access This article is licensed under a Creative Commons Attribution 4.0 International License, which permits use, sharing, adaptation, distribution and reproduction in any medium or format, as long as you give appropriate credit to the original author(s) and the source, provide a link to the Creative Commons license, and indicate if changes were made. The images or other third party material in this article are included in the article's Creative Commons license, unless indicated otherwise in a credit line to the material. If material is not included in the article's Creative Commons license and your intended use is not permitted by statutory regulation or exceeds the permitted use, you will need to obtain permission directly from the copyright holder. To view a copy of this license, visit <http://creativecommons.org/licenses/by/4.0/>.

© The Author(s) 2022